

ARTICLE OPEN



Orbital design of Berry curvature: pinch points and giant dipoles induced by crystal fields

Maria Teresa Mercaldo ¹✉, Canio Noce ^{1,2}, Andrea D. Caviglia ³, Mario Cuoco ² and Carmine Ortix ¹✉

The Berry curvature (BC)—a quantity encoding the geometric properties of the electronic wavefunctions in a solid—is at the heart of different Hall-like transport phenomena, including the anomalous Hall and the non-linear Hall and Nernst effects. In non-magnetic quantum materials with acentric crystalline arrangements, local concentrations of BC are generally linked to single-particle wavefunctions that are a quantum superposition of electron and hole excitations. BC-mediated effects are consequently observed in two-dimensional systems with pairs of massive Dirac cones and three-dimensional bulk crystals with quartets of Weyl cones. Here, we demonstrate that in materials equipped with orbital degrees of freedom local BC concentrations can arise even in the complete absence of hole excitations. In these solids, the crystal fields appearing in very low-symmetry structures trigger BCs characterized by hot-spots and singular pinch points. These characteristics naturally yield giant BC dipoles and large non-linear transport responses in time-reversal symmetric conditions.

npj Quantum Materials (2023)8:12; <https://doi.org/10.1038/s41535-023-00545-y>

INTRODUCTION

Quantum materials can be generally defined as those solid-state structures hosting physical phenomena which, even at the macroscopic scale, cannot be captured by a purely classical description¹. Among such quantum phenomena, those related to the geometric properties of the electronic wavefunctions play undoubtedly a primary role. In an N -band crystalline system, the cell-periodic part of the electronic Bloch waves defines a mapping from the Brillouin zone (BZ) to a complex space naturally equipped with a geometric structure—its tangent space defines a Fubini-Study metric² that measures the infinitesimal distance between Bloch states at different points of the BZ. The imaginary part of this quantum geometric tensor^{3,4} corresponds to the well-known Berry curvature (BC), which, when integrated over the full BZ, gives the Chern number cataloging two-dimensional insulators⁵. In metallic systems with partially filled bands, the BC summed over all occupied states can result in a non-vanishing Berry phase if the system breaks time-reversal symmetry. This Berry phase regulates the intrinsic part of the anomalous Hall conductivity of magnetic metals^{6–9}.

Materials with an acentric crystal structure can possess non-vanishing concentrations of BC even if magnetic order is absent. Probing the BC of these non-centrosymmetric and non-magnetic materials via charge transport measurements usually requires externally applied magnetic fields. For instance, in time-reversal invariant Weyl semimetals, such as TaAs¹⁰, the strong BC arising from the Weyl nodes can be revealed using the planar Hall effect¹¹—a physical consequence of the negative longitudinal magnetoresistance associated with the chiral anomaly of Weyl fermions¹². Recently, it has been also shown that the planar Hall effect can display an anomalous antisymmetric response^{13,14}, which, at least in two-dimensional materials, is entirely due to an unbalance in the BC distribution triggered by the Zeeman-induced spin splitting of the electronic bands.

In the absence of external magnetic fields, a BC charge transport diagnostic for non-magnetic materials requires to go

beyond the linear response regime^{15–19}. Hall-like currents appearing as a non-linear (quadratic) response to a driving electric field can have an intrinsic contribution governed by the Berry curvature dipole (BCD), which is essentially the first moment of the Berry curvature in momentum space. In three-dimensional systems, non-vanishing BCDs have been linked to the presence of tilted Weyl cones, and have been shown to exist both in type-I and in type-II Weyl semimetals²⁰ such as MoTe₂²¹ and the ternary compound TaIrTe₄^{22,23}. Furthermore, the Rashba semiconductor BiTeI has been predicted to host a BCD that is strongly enhanced across its pressure-induced topological phase transitions²⁴.

In two-dimensional materials, the appearance of BCDs is subject to stringent symmetry constraints: the largest symmetry group is C_s , which is composed by the identity and a single vertical mirror line. Note that non-linear Hall currents can exist in symmetry groups containing also rotational symmetries. In these cases non-linear skew and side-jump scatterings are the origin of the phenomenon^{18,19,25}. The concomitant presence of spin-orbit coupled massive Dirac cones with substantial BC and unusually low-symmetry crystalline environments have suggested the surface states of SnTe²⁶ in the low-temperature ferroelectric phase²⁷, monolayer transition metal dichalcogenides in the so-called $1T_d$ phase^{28–30}, and bilayer WTe₂ as material structures hosting sizable BCDs^{31,32}. Spin-orbit free two-dimensional materials, including monolayer and bilayer graphene, have been also put forward as materials with relatively large BCDs³³. In these systems, it is the interplay between the trigonal warping of the Fermi surface and the presence of massive Dirac cones due to inversion symmetry breaking that triggers dipolar concentration of Berry curvatures³⁴.

Finite concentrations of BC and BCDs are symmetry allowed also in systems that do not feature quartets of Weyl cones and pairs of massive Dirac cones. The anomalous massless Dirac cones at the surface of three-dimensional strong topological insulators³⁵ as well as conventional two-dimensional electron gases (2DEG) with Rashba spin-orbit coupling³⁶ are generally characterized by finite local BC concentrations when subject to trigonal crystal fields. The existence

¹Dipartimento di Fisica 'E. R. Caianiello', Università di Salerno, 84084 Fisciano (SA), Italy. ²SPIN-CNR, c/o Università di Salerno, 84084 Fisciano (SA), Italy. ³Department of Quantum Matter Physics, University of Geneva, 24 Quai Ernest Ansermet, CH-1211 Geneva, Switzerland. ✉email: mmercald@unisa.it; cortix@unisa.it

of BC in 2DEGs, which has been experimentally probed through anomalous planar Hall effect measurements³⁶, provides a new avenue for investigations. It shows in fact that Berry curvature-mediated effects can be generated entirely from conduction electrons. This overcomes the requirement of materials with narrow gaps in which the electronic wavefunctions at the Fermi level are a quantum superposition of electron and hole excitations, and extends the palette of non-magnetic materials displaying BC effects to, for instance, doped semiconductors with gaps in the eV range. It also proves that it is possible to trigger BC effects in conventional electron liquids with competing instabilities towards other many-body quantum phases.

In a spin-orbit coupled 2DEG, the BC is however triggered by crystalline anisotropy terms, which are cubic in momentum and linked to the out-of-plane component of the spin textures^{37,38}. Consequently, the BC does not possess the characteristic ‘hot-spots’ appearing in close proximity to near degeneracy between two bands where the Bloch wavefunctions are rapidly changing. The absence of such BC hot-spots forbids, in turn, large enhancements of the BCD, which is a central quest for material design. This motivates the fundamental question on whether and how an electron system can develop strong local BC concentrations in time-reversal symmetric conditions even in the complete absence of hole excitations. Here, we provide a positive answer to this question by showing that spin-orbit free metallic systems with an effective pseudo-spin one orbital degree of freedom can display BC hot-spots and characteristic BC singular pinch points that yield dipoles order of magnitudes larger than those triggered by spin-orbit coupling in a 2DEG.

RESULTS

Model Hamiltonian from symmetry principles

Let us first consider a generic single-valley two-level system in two dimensions with spin degree of freedom only. The corresponding energy spectrum is assumed to accurately represent the electronic bands close to the Fermi level of the metal in question. As long as we consider materials without long-range magnetic order, the two Fermi surfaces must originate from one of the four time-reversal invariant point of the Brillouin zone (BZ) $(n_1\mathbf{b}_1 + n_2\mathbf{b}_2)/2$ with $\mathbf{b}_{1,2}$ the two primitive reciprocal lattice vectors of the BZ and $n_{1,2} = 0, 1$. We emphasize that our arguments hold also for systems with multiple pairs of pockets centered at time-reversal invariant momenta. Time-reversal symmetry guarantees that the two bands will be Kramers’ degenerate at the time-reversal invariant momenta (TRIM). The effective Hamiltonian in the vicinity of the TRIM can be captured using a conventional $\mathbf{k} \cdot \mathbf{p}$ theory that keeps track of the point group symmetries of the crystal. To make things concrete, let us assume that the low-energy conduction bands are centered around the Γ point of the BZ and we are dealing with an acentric crystal with C_{3v} point group symmetry. This is the largest acentric symmetry group without $C_2\mathcal{T}$ symmetry, C_2 indicating a twofold rotation symmetry with out-of-plane axis and \mathcal{T} time-reversal, and thus allows for local BC concentrations¹³. The generators of C_{3v} are the threefold rotation symmetry C_3 and a vertical mirror symmetry, which, without loss of generality, we take as \mathcal{M}_x sending $x \rightarrow -x$. The threefold rotation symmetry can be represented as $e^{-i\pi\sigma_z/3}$ while the mirror symmetry as $i\sigma_x$ ³⁹. Momentum and spin transform under C_3 and \mathcal{M}_x as follows

$$\begin{aligned} C_3 : k_{\pm} &\rightarrow e^{\pm 2\pi i/3} k_{\pm}; & \sigma_{\pm} &\rightarrow e^{\pm 2\pi i/3} \sigma_{\pm} & \sigma_z &\rightarrow \sigma_z \\ \mathcal{M}_x : k_{\pm} &\rightarrow -k_{\pm}; & \sigma_{y,z} &\rightarrow -\sigma_{y,z} & \sigma_x &\rightarrow \sigma_x \end{aligned} \quad (1)$$

where $k_{\pm} = k_x \pm ik_y$ and $\sigma_{\pm} = \sigma_x \pm i\sigma_y$. Furthermore, the Hamiltonian must satisfy the time-reversal symmetry constraint $\mathcal{H}(\mathbf{k}) = \mathcal{T}\mathcal{H}(-\mathbf{k})\mathcal{T}^{-1}$, with the time-reversal operator that, as usual, can be represented as $\mathcal{T} = i\sigma_y\mathcal{K}$ and \mathcal{K} the complex conjugation. When expanded up to linear order in \mathbf{k} , the form of the Hamiltonian reads as $\mathcal{H}(\mathbf{k}) = a_R(k_x\sigma_y - k_y\sigma_x)$. The Dirac cone

energy spectrum predicted by this Hamiltonian violates the fermion doubling theorem⁴⁰ and hence can occur only on the isolated surfaces of three-dimensional strong topological insulators⁴¹. And indeed $\mathcal{H}(\mathbf{k})$ coincides with the effective Hamiltonian for the surface states of the topological insulators in the Bi_2Se_3 material class^{39,42,43}. In a genuine two-dimensional system such anomalous states cannot be present, and an even number of Kramers’ related pair of bands must exist at each Fermi energy. Consequently, the effective Hamiltonian must be equipped with an additional term that is quadratic in momentum and such that it doubles the number of states at each energy. Time-reversal symmetry implies that terms quadratic in momentum are coupled to the identity matrix. Therefore, we arrive at the well-known Hamiltonian of a two-dimensional electron gas with Rashba-like spin-orbit coupling that reads

$$\mathcal{H}(\mathbf{k}) = \frac{\hbar^2 k^2}{2m} \sigma_0 + a_R(k_x\sigma_y - k_y\sigma_x). \quad (2)$$

The corresponding energy spectrum consisting of two shifted parabolas is schematically shown in Fig. 1a. Although the crystalline symmetry requirements are fulfilled, the Hamiltonian above does not predict any finite BC local concentration. This is because the \mathbf{d} vector associated to the Hamiltonian $\mathbf{d} = \{-a_R k_y, a_R k_x, 0\}$ is confined to a two-dimensional plane at all momenta.

There are two different ways to lift the \mathbf{d} vector out-of-plane and thus trigger a non-vanishing BC⁴⁴. The first one consists in introducing a constant mass $\Delta\sigma_z$. This term removes the Kramers’ degeneracy at the TRIM [see Fig. 1b] and therefore breaks time-reversal invariance. It can be realized by externally applying an out-of-plane magnetic field or by inducing long-range magnetic order. The BC then generally displays an hot-spot located at the TRIM and a circular symmetric distribution [see Fig. 1c]. Moreover, time-reversal symmetry breaking implies that the Berry phase accumulated by electrons on the Fermi surface is non-vanishing⁶. The second route explicitly takes into account trigonal warping terms which are cubic in momentum and couple to the Pauli matrix σ_z . Such terms preserve time-reversal invariance, and thus create a BC distribution with an angular dependence such that the Berry phase accumulated over any symmetry-allowed Fermi line cancels out³⁵. Perhaps more importantly, the BC triggered by crystalline anisotropy terms³⁶ does not display a hot-spot, thus suggesting that in systems with conventional quasiparticles and a single internal degree of freedom time-reversal symmetry breaking is a prerequisite for large local BC enhancements.

We now refute this assertion by showing that in systems with orbital degrees of freedom the formation of BC hot-spots is entirely allowed even in time-reversal symmetric conditions. Consider for instance a system of p orbitals. In a generic centrosymmetric crystal, interorbital hybridization away from the TRIM can only occur with terms that are quadratic in momentum. However, and this is key, in an acentric crystal interorbital mixing terms linear in momentum are symmetry allowed. These mixing terms, often referred to as orbital Rashba coupling^{45–47}, are able to induce BC hot spots with time-reversal symmetry, as we now show. We assume as before an acentric crystal with C_{3v} point group, and electrons that are effectively spinless due to $SU(2)$ spin symmetry conservation: we are thus removing spin-orbit coupling all together. In the p_z, p_y, p_x orbital basis, the generators of the point group are represented by

$$\mathcal{M}_x = \begin{pmatrix} 1 & 0 & 0 \\ 0 & 1 & 0 \\ 0 & 0 & -1 \end{pmatrix}; C_3 = \begin{pmatrix} 1 & 0 & 0 \\ 0 & \cos \frac{2\pi}{3} & \sin \frac{2\pi}{3} \\ 0 & -\sin \frac{2\pi}{3} & \cos \frac{2\pi}{3} \end{pmatrix},$$

The two p_{xy} orbitals form a two-dimensional irreducible representation (IRREP) whereas the p_z orbital represents a one-dimensional IRREP. The form of the effective Hamiltonian away

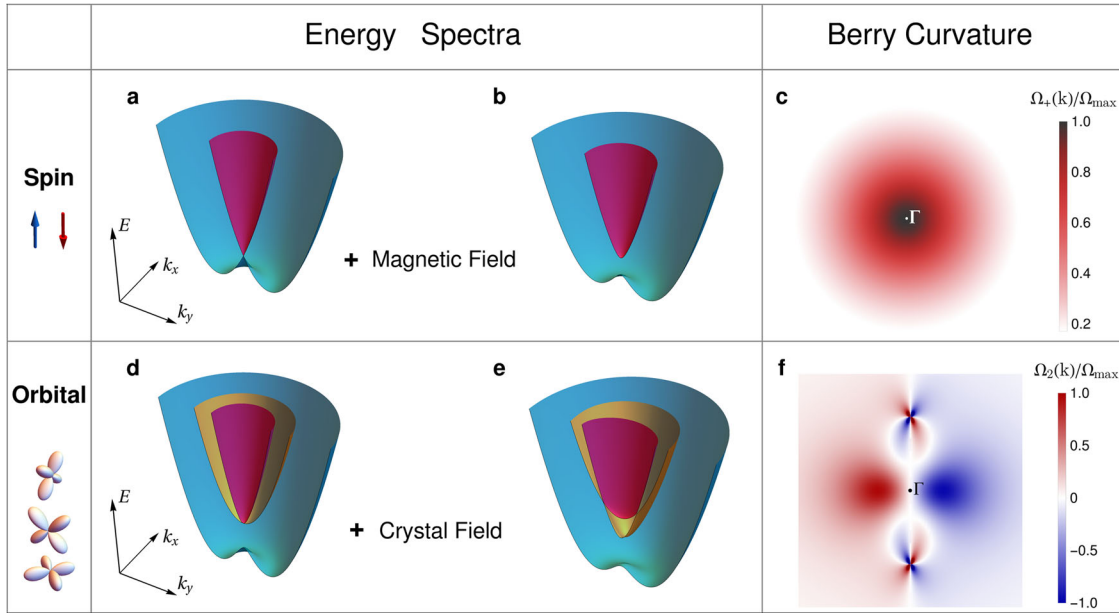


Fig. 1 Spin and orbital mechanisms of Berry curvature. **a** Schematic band structure of a two-dimensional electron gas with Rashba spin–orbit coupling. **b** An out-of-plane magnetic field breaks the Kramers' degeneracy at $\mathbf{k} = 0$ and triggers a finite BC. **c** The local BC has a circular profile with an hot spot at the Γ point of the BZ. **d** Schematic band structure of a two-dimensional electron system characterized by an $L = 1$ orbital multiplet in a trigonal crystalline environment. **e** An additional crystalline symmetry lowering splits completely the energy levels at the Γ point of the BZ even if time-reversal symmetry is preserved. The presence of mirror symmetry protects crossing at finite momenta. **f** A characteristic time-reversal symmetric BC profile with the presence of hot-spots and singular pinch points. The BC has been obtained using the model Hamiltonian Eq. (5) with $\Delta = -0.2\mathcal{E}_0$, $\Delta_m = 0.12\mathcal{E}_0$, $a_R = 1.0\mathcal{E}_0/k_F^0$ and $a_m = 0.5\mathcal{E}_0/k_F^0$ with $\mathcal{E}_0 = \hbar^2(k_F^0)^2/(2m)$ and k_F^0 a characteristic Fermi wavevector.

from the TRIM can be captured using symmetry constraints. Specifically, any generic 3×3 Hamiltonian can be expanded in terms of the nine Gell–Mann matrices⁴⁸ Λ_i [see “Methods”] as

$$\mathcal{H}(\mathbf{k}) = \sum_{i=0}^8 b_i(\mathbf{k})\Lambda_i. \quad (3)$$

The invariance of the Hamiltonian requires that the components of the Hamiltonian vector $\mathbf{b}(\mathbf{k})$ should have the same behavior as the corresponding Gell–Mann matrices Λ_i . This means that they should belong to the same representation of the crystal point group⁴⁹. From the representation of the Λ_i 's [see “Methods” and Table 1] and those of the polynomials of \mathbf{k} [see Table 1], we find that the effective Hamiltonian up to linear order in momentum reads as

$$\mathcal{H}(\mathbf{k}) = \Delta \left(\Lambda_3 + \frac{1}{\sqrt{3}} \Lambda_8 \right) - a_R [k_x \Lambda_5 + k_y \Lambda_2]. \quad (4)$$

Here the parameter Δ quantifies the energetic splitting between the p_{xy} doublet and the p_z singlet. The second term in the Hamiltonian corresponds instead to the pseudo-spin one massless Dirac Hamiltonian^{50,51} predicted to occur for instance in the kagome lattice with a staggered magnetic π flux⁵⁰. Pseudo-spin one Dirac fermions are not subject to any fermion multiplication theorem⁵². Therefore, a doubling of the number of states at each energy is not strictly required. However, since we are interested in systems without the concomitant presence of electrons and holes, we will introduce a term $\hbar^2 k^2 \Lambda_0 / (2m)$ with an equal effective mass for all three bands. The ensuing Hamiltonian can be then seen as a generalization of the Rashba 2DEG to an $SU(3)$ system with the effect of the trigonal crystal field that leads to a partial splitting of the energy levels at the TRIM, entirely allowed by the absence of Kramers' theorem. Despite the spectral properties [c.f. Fig. 1d] have a strong resemblance to those obtained in a time-reversal broken 2DEG, a direct computation [see Methods] shows that the BC associated to the Hamiltonian above is vanishing for all momenta. Breaking time-reversal symmetry

Table 1. Character tables^a for the point groups C_{3v} and C_s .

C_{3v}	E	$2C_3$	$2\sigma_v$	Polynomials of \mathbf{k}	Gell–Mann matrices
A_1	1	1	1	$1, k_x^2 + k_y^2$	$\Lambda_3 + \Lambda_8/\sqrt{3}, \Lambda_0$
A_2	1	1	-1	-	Λ_7
E	2	-1	0	$\{k_x, k_y\}$	$\{\Lambda_1, \Lambda_4\}, \{\Lambda_2, \Lambda_5\}$ $\{\Lambda_6, \Lambda_3/2 - \sqrt{3}\Lambda_8/2\}$
C_s	E	$2\sigma_v$	Polynomials of \mathbf{k}	Gell–Mann matrices	
A'	1	1	$1, k_y, k_x^2, k_y^2$	$\Lambda_1, \Lambda_2, \Lambda_3, \Lambda_8$	
A''	1	-1	k_x	$\Lambda_4, \Lambda_5, \Lambda_6, \Lambda_7$	

^aWe indicate the representation of the Gell–Mann matrices and the polynomials of momentum \mathbf{k} . The model Hamiltonians reported in the main text can be obtained by additionally using the time-reversal symmetry constraint $\mathcal{H}^*(-k_x, -k_y) = \mathcal{H}(k_x, k_y)$.

introducing a constant mass term $\propto \Lambda_7$ or considering crystalline anisotropy terms that are cubic in momentum represent two possible routes to trigger a finite Berry curvature. The crux of the story is that in the present $SU(3)$ system at hand, another possibility exists. It only relies on the crystal field effects that are generated by lowering the crystalline point group to C_s . From the representations of the Gell–Mann matrices and the polynomials of \mathbf{k} in this group, we find that the effective Hamiltonian reads

$$\mathcal{H}(\mathbf{k}) = \frac{\hbar^2 k^2}{2m} \Lambda_0 + \Delta \left(\Lambda_3 + \frac{1}{\sqrt{3}} \Lambda_8 \right) + \Delta_m \left(\frac{1}{2} \Lambda_3 - \frac{\sqrt{3}}{2} \Lambda_8 \right) - a_R [k_x \Lambda_5 + k_y \Lambda_2] - a_m k_x \Lambda_7. \quad (5)$$

Nothing prevents to have the interorbital mixing terms $\propto \Lambda_{2,5}$ with different amplitudes. Without loss of generality, in the remainder we

will consider a single parameter a_R . In the Hamiltonian above, we have also neglected a constant term $\propto \Lambda_1$. For materials with an high-temperature trigonal structure, its amplitude Δ_1 is expected to be of the same order of magnitude as Δ_m . In this regime [see the Supplementary Note 1], a term $\propto \Lambda_1$ has a very weak effect on the energy spectrum and BC properties, and can be thus disregarded. The energy spectrum reported in Fig. 1e shows that the effect of the crystal symmetry lowering is twofold. First, there is an additional energy splitting between the p_{xy} implying that all levels at the Γ point of the BZ are singly degenerate. Second, the two p_{xy} orbitals have band degeneracies along the mirror symmetric $k_x = 0$ line of the BZ. Such mirror-symmetry protected crossings give rise to BC singular pinch points [see Fig. 1f and the Supplementary Note 2]. It is the presence of these pinch points that represents the hallmark of the non-trivial geometry of the electronic wavefunctions associated with the p -orbital manifold. Note that the BC also displays hot-spots [see Fig. 1f] with BC sources and sinks averaging to zero on any mirror symmetric Fermi surface as mandated by time-reversal invariance.

Material realizations

Before analyzing the origin and physical consequence of the BC and its characteristic pinch points, we now introduce a material platform naturally equipped with orbital degrees of freedom and the required low crystalline symmetry: [111] interfaces of transition metal oxides hosting two-dimensional d electron systems of t_{2g} orbital character such as SrTiO₃^{53,54}, KTaO₃⁵⁵, and SrVO₃-based heterostructures. When compared to conventional semiconductor heterostructures, complex oxide interfaces consist of d electrons with different symmetries, a key element in determining their many-body ground states that include, notably, unconventional superconductivity⁵⁶. In the high-temperature cubic phases of these materials, the octahedral crystal field pins the low-energy physics to a degenerate t_{2g} manifold, which spans an effective angular momentum one subspace, precisely as the p orbitals discussed above. We note that for the t_{2g} orbitals the spin-orbit coupling has a minus sign due to the effective orbital moment projection from $L = 2$ to the $L_{\text{eff}} = 1$ in the t_{2g} manifold. This overall sign however is not altering the results. The reduced symmetry at interfaces lift the t_{2g} energetic degeneracy and modify their orbital character. At the [111] interface the transition metal atoms form a stacked triangular lattice with three interlaced layers [see Fig. 2a, b]. This results in a triangular planar crystal field that hybridizes the $|xy\rangle$, $|xz\rangle$ and $|yz\rangle$ orbitals to form an $|a_{1g}\rangle = (|xy\rangle + |xz\rangle + |yz\rangle)/\sqrt{3}$ one-dimensional IRREP whereas the two states $|e'_{g\pm}\rangle = (|xy\rangle + \omega^{\pm 1}|xz\rangle + \omega^{\pm 2}|yz\rangle)/\sqrt{3}$, with $\omega = e^{2\pi i/3}$, form the two-dimensional IRREP.

The energetic ordering of the levels depends on the microscopic details of the interface. For example, at the (111) LaAlO₃/SrTiO₃ interface, x-ray absorption spectroscopy⁵⁷ sets the $|a_{1g}\rangle$ state at lower energy [see Fig. 2e]. By further considering the structural inversion symmetry inherently present at the hetero-interface, we thus formally reach the situation we discussed for the set of p orbitals, be it for the trigonal symmetry that excludes any local concentrations of BC. However, and this is key, low-temperature phase transitions in oxides lower the crystal symmetry, often realizing a tetragonal or orthorhombic phase with oxygen octahedra rotations and (anti)polar cation displacements. Let us consider the paradigmatic case of SrTiO₃. A structural transition occurring at around 105 K, from the cubic phase to a tetragonal structure⁵⁸ [see Fig. 2c], breaks the threefold rotational symmetry leaving a single residual mirror line. Assuming the tetragonal axis to be along the [001] direction, the surviving mirror symmetry at the [111] interface corresponds to $\mathcal{M}_{[\bar{1}10]}$ [see Fig. 2d]. This structural distortion lifts the degeneracy of the e'_g doublet. The bonding and antibonding states $|e'_{g+}\rangle \pm |e'_{g-}\rangle$ have

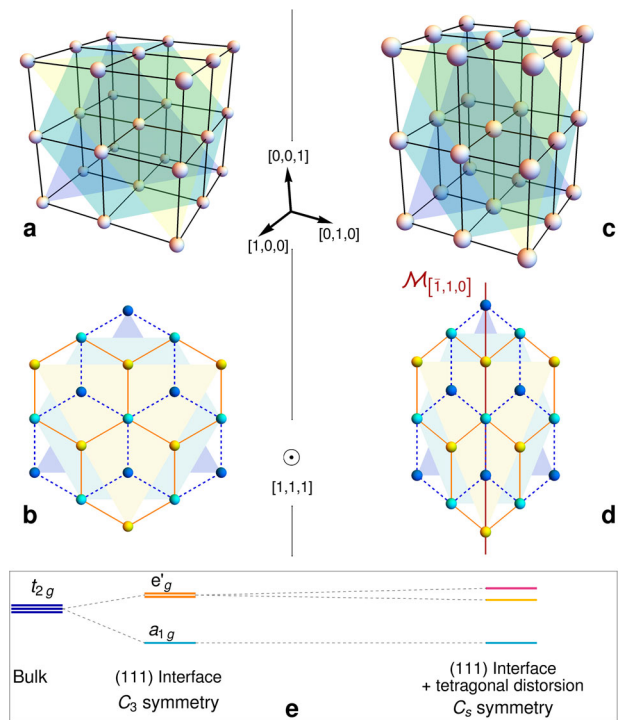


Fig. 2 Materials, crystal symmetries and orbital splittings. **a** Schematic representation of an ABO₃ perovskite cubic unit cell displaying the three interlaced transition metal [111] planes. **b** Corresponding top view along the [111] crystallographic direction. We only show the B transition metal atoms. **c, d** show the effect of a tetragonal distortion with the [001] direction being the tetragonal axis. The distortion breaks the threefold rotation symmetry around the [111] axis but leaves a residual mirror symmetry. **e** Evolution of the orbital states at the Γ point of the BZ with quenched angular momentum.

opposite mirror $\mathcal{M}_{[\bar{1}10]}$ eigenvalues and realize two distinct one-dimensional IRREP [see Fig. 2e]. SrTiO₃-based heterointerfaces undergo additional tetragonal to locally triclinic structural distortions at temperatures below $\simeq 70$ K, which involves small displacements of the Sr atoms along the [111] directions convoluted with TiO₆ oxygen-octahedron antiferrodistortive rotations⁵⁹. In addition, below about 50 K, SrTiO₃ and KTaO₃ approach a ferroelectric instability that is accompanied by strong polar quantum fluctuations. This regime is characterized by a soft transverse phonon mode that involves off-center displacement of the Ti ions with respect to the surrounding octahedron of oxygen ions⁶⁰, which, in the static limit, would correspond to a ferroelectric order parameter. This can potentially enhance the interorbital hybridization terms allowed in acentric crystalline environments, and thus boost the appearance of large BC concentrations.

Berry curvature dipole

Having identified (111)-oriented oxide heterointerfaces as ideal material platforms, we next analyze the specific properties of the BC and its first moment. We first notice that in the case of a two-level spin system the local Berry curvature of the spin-split bands, if non-vanishing, is opposite. Due to the concomitant presence of both spin-bands at each Fermi energy, the spin split bands cancel their respective local BC except for those momenta which are occupied by one spin band. In the SU(3) system at hand, there is a similar sum rule stating that at each momentum \mathbf{k} the BC of the three bands [c.f. Fig. 3a] sum to zero. However, and as mentioned above, the orbital bands are not subject to fermion multiplication theorems. In certain energy ranges a single orbital band is

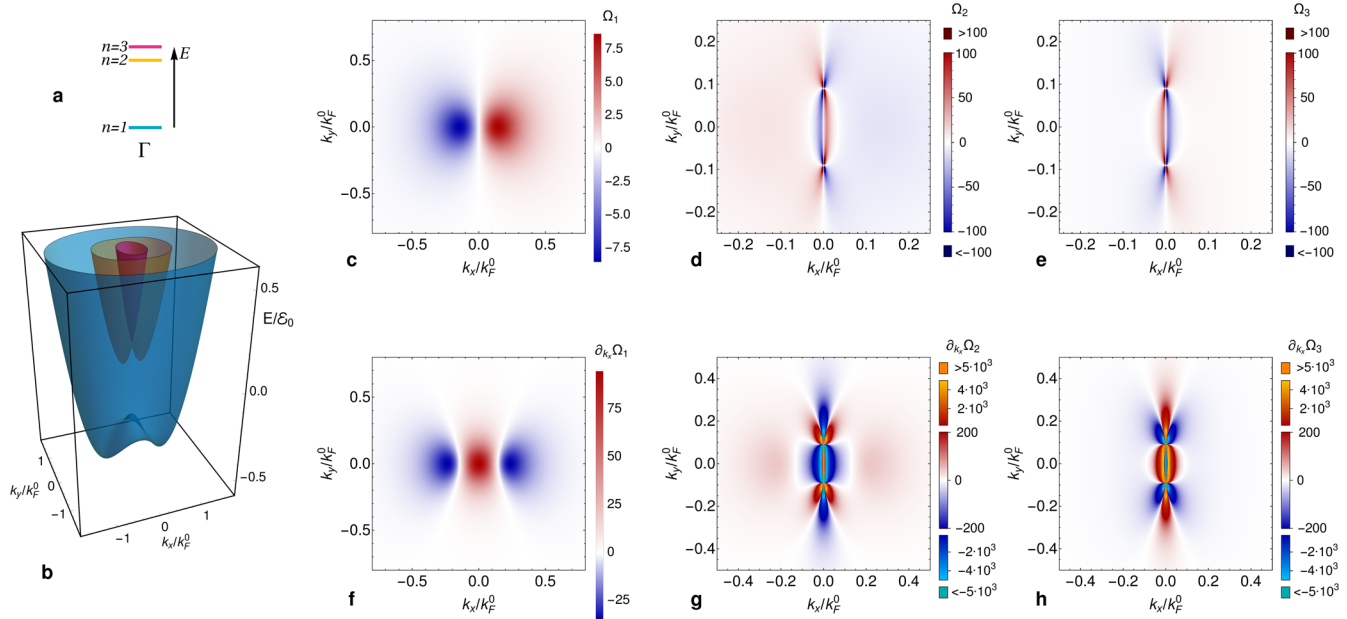


Fig. 3 Orbital design of Berry curvature hot-spots and pinch points. **a** Ordering of the crystal field split t_{2g} (p) orbitals with their associated band index. **b** Energy spectrum of the model Eq. (5) obtained using the parameter set $\Delta = -0.2\mathcal{E}_0$, $\Delta_m = 0.01\mathcal{E}_0$, $a_R = a_m = 1.0\mathcal{E}_0/k_F^0$. **c–e** show the ensuing band-resolved Berry curvature. **f–h** are the corresponding BC dipole densities $\partial_{k_x}\Omega$. Note that the presence of mirror symmetry guarantees that the orthogonal dipole density $\partial_{k_y}\Omega$ averages to zero.

occupied [c.f., Fig. 3a, b] and BC cancellations are not at work. There is also another essential difference between the BC associated to spin and orbital degrees of freedom. In general, the commutation and anticommutation relations of the $SU(N)$ Lie algebra define symmetric and antisymmetric structure constants, which, in turn, define the star and cross products of generic $SU(N)$ vectors⁶¹. Differently from an $SU(3)$ system spanning an angular momentum one subspace, in $SU(2)$ spin systems the symmetric structure constant vanishes identically. The ensuing absence of star products $\mathbf{b}_\mathbf{k} \star \mathbf{b}_\mathbf{k}$ precludes the appearance of BC with time-reversal symmetry as long as crystalline anisotropies are not taken into account [see “Methods”]. On the other hand, for $SU(3)$ the presence of all three purely imaginary Gell–Mann matrices $\Lambda_{2,5,7}$, together with the “mass” terms $\Lambda_{3,8}$, is a sufficient condition to obtain time-reversal symmetric BC concentrations even when accounting only for terms that are linear in momentum [see “Methods”]. This, however, strictly requires that all rotation symmetries must be broken.

Next, we analyze the properties of the band resolved local BC starting from the lowest energy band, which corresponds to the $(|xy\rangle + |xz\rangle + |yz\rangle)/\sqrt{3}$ state at (111) LAO/STO heterointerfaces. Figure 3c shows a characteristic BC profile. It displays two opposite poles centered on the $k_y = 0$ line. These sources and sinks of BC are equidistant from the mirror symmetric $k_x = 0$ line since the BC, as any genuine pseudoscalar, must be odd under vertical mirror symmetry operations, i.e., $\Omega(k_x, k_y) = -\Omega(-k_x, k_y)$. Note that the combination of time-reversal symmetry and vertical mirror implies that the BC will be even sending $k_y \rightarrow -k_y$, thus guaranteeing that, taken by themselves, the BC hot-spots will be centered around the $k_y = 0$ line. Their finite k_x values coincide with the points where the (direct) energy gap between the $n = 1$ and the $n = 2$ bands is minimized [see Fig. 3a, b and Supplementary Note 2], and thus the interorbital mixing is maximal. The properties of the BC are obviously reflected in the BCD local density $\partial_{k_x}\Omega(k_x, k_y)$: it possesses [see Fig. 3f] a positive area strongly localized at the center of the BZ that is neutralized by two mirror symmetric negative regions present at finite k_x . Let us next consider the Berry curvature profile arising from the two degenerate e'_g states that are split by the threefold rotation symmetry breaking. Fig. 3d

shows the BC profile of the lowest energy band: it is entirely dominated by the BC pinch points induced by the mirror symmetry protected degeneracies on the $k_x = 0$ line. The BC also displays a nodal ring around the pinch point, and thus possesses a characteristic d-wave character around the singular point. This can be understood by constructing a $\mathbf{k} \cdot \mathbf{p}$ theory around each of the two time-reversal related degeneracies. To do so, we first recall that the two bands deriving from the e'_g states have opposite \mathcal{M}_x mirror eigenvalue along the full mirror line $k_x \equiv 0$ of the BZ. Close to the degeneracies, \mathcal{M}_x can be therefore represented as σ_z . Under \mathcal{M}_x , $k_x \rightarrow -k_x$, whereas $k_y \rightarrow k_y$. Moreover, the Pauli matrices $\sigma_{x,y} \rightarrow -\sigma_{x,y}$. An effective two-band model close to the degeneracies must then have the following form at the leading order:

$$\mathcal{H}_{\text{eff}} = v_x k_x \sigma_x + \beta k_x \delta k_y \sigma_y + v_y \delta k_y \sigma_z, \quad (6)$$

where δk_y is the momentum measured relatively to the mirror symmetry-protected degeneracy and we have neglected the quadratic term coupling to the identity $k^2 \sigma_0$ that does not affect the BC. Using the usual formulation of the BC for a two-band model [see the “Methods” section], it is possible to show that the Hamiltonian above is characterized by a zero-momentum pinch-point with two nodal lines [see the Supplementary Note 2] and d-wave character. It is interesting to note that this also implies that the effective time-reversal symmetry inverting the sign of \mathbf{k} around the pinch point is broken. Perhaps even more importantly, the d-wave character implies a very large BCD density in the immediate neighborhood of the pinch point [see Fig. 3g]. Similar properties are encountered when considering the highest energy band, with the difference that the pinch-point has an opposite angular dependence [see Fig. 3e] and consequently the BCD density has opposite sign [c.f., Fig. 3h].

Having the band-resolved BC and BCD density profiles in our hands, we finally discuss their characteristic fingerprints in the BCD defined by $D_x = \int_{\mathbf{k}} \partial_{k_x} \Omega(\mathbf{k}) f_0$, with $\int_{\mathbf{k}} = \int d^2k / (2\pi)^2$ and f_0 being the equilibrium Fermi-Dirac distribution function. By continuously sweeping the Fermi energy, we find that the BCD shows cusps and inflection points [see Fig. 4a], which, as we now discuss, are a direct consequence of Lifshitz transitions and

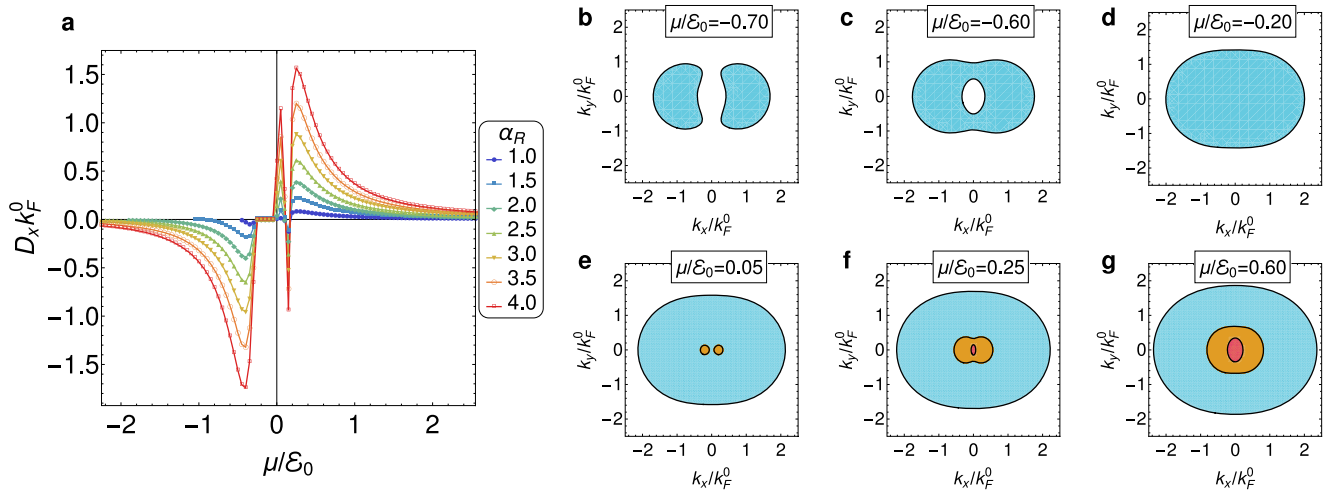


Fig. 4 Berry curvature dipole and topology of the Fermi lines. **a** Behavior of the Berry curvature dipole obtained by changing the chemical potential μ measured in units of \mathcal{E}_0 . The different curves correspond to the different values of a_R measured in units of \mathcal{E}_0/k_F^0 . The other model parameters have been instead fixed as $\Delta = -0.2\mathcal{E}_0$, $\Delta_m = -0.01\mathcal{E}_0$, $a_m = a_R$. **b–f** display the Fermi lines and the band-resolved occupied regions in momentum space for $a_R = a_m = 1.5\mathcal{E}_0/k_F^0$.

their associated van Hove singularities [see the Supplementary Note 3]. Starting from the bottom of the first band, the magnitude of the BCD continuously increases until it reaches a maximum where the dipole is larger than the inverse of the Fermi momentum of a 2DEG $1/k_F^0$ and thus gets an enhancement of three order of magnitudes with respect to a Rashba 2DEG³⁶. In this region, there are two distinct Fermi lines encircling electronic pockets at finite values of \mathbf{k} [c.f., Fig. 4b], which subsequently merge on two disconnected regions in momentum space [c.f. Fig. 4c]. Since the states in the immediate vicinity of the center of the BZ are not occupied, the BCD is entirely dominated by the two mirror symmetric negative hot-spots of Fig. 3f. By further increasing the chemical potential, the internal Fermi line collapses at the Γ point and therefore a first Lifshitz transition occurs [c.f. Fig. 4d]. In this regime, the BCD has exponentially small values due to the fact that the strong positive BCD density area around the center of the BZ counteracts the mirror symmetric negative hot-spots. By further increasing the chemical potential, a second Lifshitz transition signals the occupation of the first e_g band with two pockets centered around the $k_y=0$ line [see Fig. 4e]. This Lifshitz transition coincides with a rapid increase of the BCD due to the contribution coming from the local BCD density regions external to the BC nodal ring of Fig. 3g. The subsequent sharp negative peak originates from a third Lifshitz transition in which the two electronic pockets of the second band merge, and almost concomitantly a tiny pocket of the third band centered around Γ arises [see Fig. 4f]. By computing the band resolved BCD [see the Supplementary Note 4] one finds that it is this small pocket the cause of the negative sharp peak. For large enough chemical potentials, the BCD develops an additional peak corresponding to the fermiology of Fig. 4g. This peak, which is again larger than $1/k_F^0$, can be understood by noticing that due to the BC local sum rule the momenta close to the center of the BZ do not contribute to the BCD. On the other hand, the regions external to the BC nodal ring are unoccupied by the third band and consequently have a net positive BCD local density. Thermal smearing can affect the strongly localized peaks at lower chemical potential but will not alter the presence of this broader peak. Note that the BCD gets amplified by increasing the interorbital mixing parameters a_R, a_m but retains similar properties [see Fig. 4 and the Supplementary Note 3]. The strength of BC-mediated effects depends indeed on the ratio between the characteristic orbital Rashba energy

$2ma_{R(m)}^2/\hbar^2$ and the crystal field splittings $\Delta_{(m)}$. The BCD properties and values comparable to the Fermi wavelength are hence completely generic.

Let us finally discuss the role of spin–orbit coupling. It can be included in our model Hamiltonian Eq. (5) as $\mathcal{H}_{so} = \lambda_{so}(L_x \otimes \tau_x + L_y \otimes \tau_y + L_z \otimes \tau_z)$, where λ_{so} is the spin–orbit coupling strength, the $L=1$ angular momentum matrices correspond to the Gell–Mann matrices $\Lambda_2, \Lambda_5, \Lambda_7$, and the Pauli matrices $\tau_{x,y,z}$ act in spin space. Its effect can be analyzed using conventional (degenerate) perturbation theory. At the center of the Brillouin zone, \mathcal{H}_{so} is completely inactive—the eigenstates of the Hamiltonian Eq. (5) are orbital eigenstates and the off-diagonal terms in orbital space $\Lambda_{2,5,7}$ cannot give any correction at first order in λ_{so} . The situation is different at finite values of momentum. The two spin–orbit free degenerate eigenstates are a superposition of the different orbitals (due to the orbital Rashba coupling). Therefore, the spin–orbit coupling term will lift their degeneracy resulting in a Rashba-like splitting of the bands.

In order to explore the consequence of this spin splitting on the Berry curvature, let us denote with $|\psi_0^\uparrow(\mathbf{k})\rangle$ and $|\psi_0^\downarrow(\mathbf{k})\rangle$ the two spin–orbit free degenerate eigenstates at each value of the momentum. Note that $|\psi_0\rangle$ is a three-component spinor for the orbital degrees of freedom. When accounting perturbatively for spin–orbit coupling the eigenstates will be a superposition of the spin degenerate eigenstates and will generally read

$$|\psi^+(\mathbf{k})\rangle = \cos\theta(\mathbf{k})e^{i\phi(\mathbf{k})}|\psi_0^\uparrow(\mathbf{k})\rangle + \sin\theta(\mathbf{k})|\psi_0^\downarrow(\mathbf{k})\rangle$$

$$|\psi^-(\mathbf{k})\rangle = -\sin\theta(\mathbf{k})e^{i\phi(\mathbf{k})}|\psi_0^\uparrow(\mathbf{k})\rangle + \cos\theta(\mathbf{k})|\psi_0^\downarrow(\mathbf{k})\rangle$$

Here, the momentum dependence of the phase ϕ and the angle θ is a by-product of the orbital Rashba coupling: the effect of spin–orbit coupling, which is off-diagonal in orbital space, is modulated by the momentum-dependent orbital content of the eigenstates $|\psi_0^{\uparrow,\downarrow}(\mathbf{k})\rangle$. The abelian Berry connection of the two spin-split states $\mathcal{A}_{k_x, k_y}^{+-} = \langle \psi^{+-}(\mathbf{k}) | i\partial_{k_x, k_y} \psi^{+-}(\mathbf{k}) \rangle$ will therefore contain two terms: the first one is the spin-independent Berry connection $\mathcal{A}_{k_x, k_y}^0 = \langle \psi_0(\mathbf{k}) | i\partial_{k_x, k_y} \psi_0(\mathbf{k}) \rangle$; the second term is instead related to the derivatives of the phase ϕ and angle θ . This Berry connection is opposite for the $+, -$ states and coincides with the Berry connection of a two-level spin system⁴⁴. This also implies that the Berry curvature of the Kramers' pair of bands $\Omega^{+-}(\mathbf{k}) = \Omega(\mathbf{k}) \pm \Omega_{so}(\mathbf{k})$. The contribution of the Berry curvature

Ω_{s_0} is opposite for the time-reversed partners and the net effect only comes from the difference between the Fermi lines of two partner bands. However, the purely orbital Berry curvature $\Omega(\mathbf{k})$, which can be calculated directly from Eq. (5), sums up. The values of the BCD presented in Fig. 4 are thus simply doubled in the presence of a weak but finite spin-orbit coupling.

DISCUSSION

In this study, we have shown an intrinsic pathway to design large concentrations of Berry curvature in time-reversal symmetric conditions making use only of the orbital angular momentum electrons acquire when bound to atomic nuclei. Such mechanism is different in nature with respect to that exploited in topological semimetals and narrow-gap semiconductors where the geometric properties of the electronic wavefunctions originate from the coupling between electron and hole excitations. The orbital design of Berry curvature is also inherently different from the time-reversal symmetric spin-orbit mechanism^{35,36}, which strongly relies on crystalline anisotropy terms. We have shown in fact that the Berry curvature triggered by orbital degrees of freedom features both hot-spots and singular pinch-points. Furthermore, due to the crystalline symmetry constraints the Berry curvature is naturally equipped with a non-vanishing Berry curvature dipole. These characteristics yield a boost of three orders of magnitude in the quantum non-linear Hall effect. In (111) LaAlO₃-SrTiO₃ heterointerfaces where the characteristic Fermi wavevector $k_F^0 \simeq 1 \text{ nm}^{-1}$, the Berry curvature dipole $D_x \simeq 1 \text{ nm}$. The corresponding non-linear Hall voltage can be evaluated using the relation^{31,33} $V_{yxx} = e^3 \tau D_x |I_x|^2 / (2\hbar^2 \sigma_{xx}^2 W)$, with the characteristic relaxation time $\tau \simeq 1 \text{ pS}$ and the longitudinal conductance $\sigma_{xx} \simeq 5 \text{ mS}$. In a typical Hall bar of width $W \simeq 10 \mu\text{m}$ sourced with a current $I_x \simeq 100 \mu\text{A}$, the non linear Hall voltage $V_{yxx} \simeq 2 \mu\text{V}$, which is compatible with the strong non-linear Hall signal experimentally detected³⁶.

The findings of our study carry a dramatic impact on the developing area of condensed matter physics dubbed orbitronics⁶². Electrons in solids can carry information by exploiting either their intrinsic spin or their orbital angular momentum. Generation, detection and manipulation of information using the electron spin is at the basis of spintronics. The Berry curvature distribution we have unveiled in our study is expected to trigger also an orbital Hall effect, whose origin is rooted in the geometric properties of the electronic wavefunctions, and can be manipulated using the orbital degrees of freedom. This opens a number of possibilities for orbitronic devices. This is even more relevant considering that our findings can be applied to a wide class of materials whose electronic properties can be described with an effective $L = 1$ orbital multiplet. These include other complex oxide heterointerfaces as well as spin-orbit free semiconductors where p -orbitals can be exploited. Since Dirac quasiparticles are not required in the orbital design of Berry curvature, it is possible to reach carrier densities large enough to potentially exploit electron-electron and electron-phonon interactions effects in the control of Berry curvature-mediated effects. For instance, orbital selective metal-insulator transitions can be used to switch on and off the electronic transport channels responsible for the Berry curvature and its dipole. We envision that this capability can be used to design orbitronic and electronic transistors relying on the geometry of the quantum wavefunctions.

METHODS

Representation of the Gell-Mann matrices in the symmetry groups

Apart from the identity matrix Λ_0 , the eight Gell-Mann matrices can be defined as

$$\begin{aligned} \Lambda_1 &= \begin{pmatrix} 0 & 1 & 0 \\ 1 & 0 & 0 \\ 0 & 0 & 0 \end{pmatrix}, & \Lambda_2 &= \begin{pmatrix} 0 & -i & 0 \\ i & 0 & 0 \\ 0 & 0 & 0 \end{pmatrix}, \\ \Lambda_3 &= \begin{pmatrix} 1 & 0 & 0 \\ 0 & -1 & 0 \\ 0 & 0 & 0 \end{pmatrix}, & \Lambda_4 &= \begin{pmatrix} 0 & 0 & 1 \\ 0 & 0 & 0 \\ 1 & 0 & 0 \end{pmatrix}, \\ \Lambda_5 &= \begin{pmatrix} 0 & 0 & -i \\ 0 & 0 & 0 \\ i & 0 & 0 \end{pmatrix}, & \Lambda_6 &= \begin{pmatrix} 0 & 0 & 0 \\ 0 & 0 & 1 \\ 0 & 1 & 0 \end{pmatrix}, \\ \Lambda_7 &= \begin{pmatrix} 0 & 0 & 0 \\ 0 & 0 & -i \\ 0 & i & 0 \end{pmatrix}, & \Lambda_8 &= \begin{pmatrix} \frac{1}{\sqrt{3}} & 0 & 0 \\ 0 & \frac{1}{\sqrt{3}} & 0 \\ 0 & 0 & -\frac{2}{\sqrt{3}} \end{pmatrix}. \end{aligned}$$

Let us now check the properties of these eight Gell-Mann matrices under time-reversal symmetry. Since we are considering electrons that are effectively spinless due to the $SU(2)$ spin symmetry, the time-reversal operator can be represented as \mathcal{K} . Hence, the three Gell-Mann matrices $\Lambda_2, \Lambda_5, \Lambda_7$ are odd under time-reversal, i.e., $\mathcal{T}^{-1} \Lambda_{2,5,7} \mathcal{T} = -\Lambda_{2,5,7}$, whereas the remaining matrices are even under time-reversal. Similarly, $\Lambda_{1,2,3,8}$ are even under the vertical mirror symmetry whereas $\Lambda_{4,5,6,7}$ are odd. Let us finally talk about the threefold rotational symmetry. Since the rotation symmetry operator $\mathcal{C}_3 = \exp[2\pi i \Lambda_7 / 3]$, the transformation properties of the Gell-Mann matrices are determined by the commutation relations $[\Lambda_7, \Lambda_i]$. The commutation relations are listed as follows:

$$\begin{aligned} [\Lambda_7, \Lambda_1] &= i\Lambda_4 & [\Lambda_7, \Lambda_2] &= i\Lambda_5 \\ [\Lambda_7, \Lambda_4] &= -i\Lambda_1 & [\Lambda_7, \Lambda_5] &= -i\Lambda_2 \\ [\Lambda_7, \Lambda_6] &= 2i\left(\frac{\Lambda_3}{2} - \frac{\sqrt{3}}{2}\Lambda_8\right) & [\Lambda_7, \frac{\Lambda_3}{2} - \frac{\sqrt{3}}{2}\Lambda_8] &= -2i\Lambda_6 \\ [\Lambda_7, \Lambda_3 + \frac{\Lambda_8}{\sqrt{3}}] &= 0 \end{aligned}$$

The results above indicate that the three pairs of operators $\{\Lambda_1, \Lambda_4\}$, $\{\Lambda_2, \Lambda_5\}$, and $\{\Lambda_6, \frac{\Lambda_3}{2} - \frac{\sqrt{3}}{2}\Lambda_8\}$ behave as vector under the threefold rotation symmetry and therefore form two-dimensional IRREPS.

Berry curvature of $SU(2)$ and $SU(3)$ systems

For $SU(2)$ systems, a generic Hamiltonian can be written in terms of Pauli matrices σ_i as $\mathcal{H}(\mathbf{k}) = d_0(\mathbf{k})\sigma_0 + \mathbf{d}(\mathbf{k}) \cdot \boldsymbol{\sigma}$, where σ_0 is the 2×2 identity matrix and the Pauli matrix vector $\boldsymbol{\sigma} = (\sigma_x, \sigma_y, \sigma_z)$. The Berry curvature can be expressed in terms of \mathbf{d} vector

$$\Omega_{\pm}(\mathbf{k}) = \mp \frac{1}{2|\mathbf{d}(\mathbf{k})|^3} \mathbf{d}(\mathbf{k}) \cdot [\partial_{k_x} \mathbf{d}(\mathbf{k}) \times \partial_{k_y} \mathbf{d}(\mathbf{k})]. \quad (7)$$

For $SU(3)$ system, we can proceed analogously using the Gell-Mann matrices introduced above. The Hamiltonian of a system described by three electronic degrees of freedom in a 3×3 manifold can be written as $\mathcal{H}(\mathbf{k}) = b_0(\mathbf{k})\Lambda_0 + \mathbf{b}(\mathbf{k}) \cdot \boldsymbol{\Lambda}$, where $b_0(\mathbf{k})$ is a scalar and $\mathbf{b}(\mathbf{k})$ is an eight-dimensional vector. The Gell-Mann matrices satisfy an algebra that is a generalization of the $SU(2)$. In particular, we have that

$$\Lambda_a \Lambda_b = \frac{2}{3} \delta_{ab} + (d_{abc} + if_{abc}) \Lambda_c, \quad (8)$$

where repeated indices are summed over. In the equation above, we have introduced the antisymmetric and symmetric structure

factors of $SU(3)$ that are defined, respectively, as

$$f_{abc} = -\frac{i}{4} \text{Tr}([\Lambda_a, \Lambda_b] \Lambda_c), \quad d_{abc} = \frac{1}{4} \text{Tr}(\{\Lambda_a, \Lambda_b\} \Lambda_c).$$

From these, one defines three bilinear operations of $SU(3)$ vectors: the dot (scalar) product $\mathbf{v} \cdot \mathbf{w} = v_a w_a$, the cross product $(\mathbf{v} \times \mathbf{w})_a = f_{abc} v_b w_c$, and the star product $(\mathbf{v} \star \mathbf{w})_a = d_{abc} v_b w_c$. The star product is a symmetric vector product which does not play any role for $SU(2)$ since $d_{abc} = 0$. Moreover, the band-resolved Berry curvature is given by^{48,61}:

$$\Omega_n(\mathbf{k}) = -4 \frac{(\gamma_{\mathbf{k},n} \mathbf{b}_{\mathbf{k}} + \mathbf{b}_{\mathbf{k}} \star \mathbf{b}_{\mathbf{k}})}{(3\gamma_{\mathbf{k},n}^2 - |\mathbf{b}_{\mathbf{k}}|^2)^3} \cdot \left\{ [\gamma_{\mathbf{k},n} \partial_{k_x} \mathbf{b}_{\mathbf{k}} + \partial_{k_x} (\mathbf{b}_{\mathbf{k}} \star \mathbf{b}_{\mathbf{k}})] \times [\gamma_{\mathbf{k},n} \partial_{k_y} \mathbf{b}_{\mathbf{k}} + \partial_{k_y} (\mathbf{b}_{\mathbf{k}} \star \mathbf{b}_{\mathbf{k}})] \right\} \quad (9)$$

where we introduced $\gamma_{\mathbf{k},n} = \frac{2}{\sqrt{3}} |\mathbf{b}_{\mathbf{k}}| \cos(\theta_{\mathbf{k}} + \frac{2\pi}{3}n)$, $\theta_{\mathbf{k}} = \frac{1}{3} \arccos \left[\frac{\sqrt{3} \mathbf{b}_{\mathbf{k}} \cdot (\mathbf{b}_{\mathbf{k}} \star \mathbf{b}_{\mathbf{k}})}{|\mathbf{b}_{\mathbf{k}}|^3} \right]$, and $\mathbf{b}_{\mathbf{k}}$ is a shorthand for $\mathbf{b}(\mathbf{k})$. Generally speaking, the Berry curvature in Eq. (9) can be split in two contributions as $\Omega_n(\mathbf{k}) = \Omega_n^{(0)}(\mathbf{k}) + \Omega_n^{(*)}(\mathbf{k})$, with $\Omega_n^{(0)}(\mathbf{k}) = -4 \frac{(\gamma_{\mathbf{k},n})^3}{(3\gamma_{\mathbf{k},n}^2 - |\mathbf{b}_{\mathbf{k}}|^2)^3} \mathbf{b}_{\mathbf{k}} \cdot [\partial_{k_x} \mathbf{b}_{\mathbf{k}} \times \partial_{k_y} \mathbf{b}_{\mathbf{k}}]$ that strongly resembles the BC expression for $SU(2)$ systems of Eq. (7). In trigonal systems described by the effective Hamiltonian in Eq. (4), we have that for any momentum \mathbf{k} and for any value of the parameters, the \mathbf{b} vector associated with the Hamiltonian is such that $(\gamma_{\mathbf{k},n} \mathbf{b}_{\mathbf{k}} + \mathbf{b}_{\mathbf{k}} \star \mathbf{b}_{\mathbf{k}})$ is always orthogonal to the vector in the curly braces in the expression of the Berry curvature Eq. (9). Hence $\Omega_n(\mathbf{k}) = 0$. On the contrary, assuming a C_3 point-group symmetry the effective Hamiltonian of Eq. (5) defines $\mathbf{b}_{\mathbf{k}} = (0, \alpha_R k_y, \Delta + \frac{1}{2} \Delta_m, 0, \alpha_R k_x, 0, \alpha_m k_x, \frac{\Delta}{\sqrt{3}} - \frac{\sqrt{3}}{2} \Delta_m)$, for which we get that $\Omega_n^{(0)}(\mathbf{k}) = 0$, and the BC is substantially given by $\Omega_n^{(*)}(\mathbf{k})$. In other words, the terms obtained by doing the star product, $\mathbf{b}_{\mathbf{k}} \star \mathbf{b}_{\mathbf{k}}$ are those that yield the non-zero BC. We point out that the BC is proportional to the combination of parameters $\alpha_R^2 \alpha_m (2\Delta + \Delta_m)$. A non-vanishing BC can be thus obtained even in the absence of the Gell–Mann matrix Λ_B . This, on the other hand, would correspond to values of the crystal field splitting $\Delta_m = 2\Delta/3$ implying a very strong distortion of the crystal from the trigonal arrangement. The presence of the constant term $\alpha \Lambda_B$ is thus essential to describe systems with a parent high-temperature trigonal crystal structure.

Calculation of the Berry curvature dipole

The first moment of the Berry curvature, the Berry curvature dipole, for each energy band n is given by $D_{x,n} = \int \frac{d^2 k}{(2\pi)^2} \partial_{k_x} \Omega_n(\mathbf{k}) f_0(\mathbf{k})$, where $f_0(\mathbf{k})$ is the equilibrium Fermi–Dirac distribution function. At zero temperature, this expression can be rewritten as a line integral over the Fermi line

$$D_{x,n} = \int \frac{d^2 k}{(2\pi)^2} \Omega_n(\mathbf{k}) \frac{\partial E_n}{\partial k_x} \delta(E_n - \mu), \quad (10)$$

where $E_n = E_n(\mathbf{k})$ ($n = 1, 2, 3$) are the energy bands and μ is the chemical potential. We have used the latter expression (10) to evaluate the BCD, where $D_x = \sum_{n=1}^3 D_{x,n}$.

DATA AVAILABILITY

The data that support the findings of this study are available from the corresponding authors upon reasonable request.

CODE AVAILABILITY

All numerical codes in this paper are available from the corresponding authors upon reasonable request.

Received: 22 August 2022; Accepted: 14 February 2023;

Published online: 28 February 2023

REFERENCES

- Keimer, B. & Moore, J. E. The physics of quantum materials. *Nat. Phys.* **13**, 1045–1055 (2017).
- Anandan, J. & Aharonov, Y. Geometry of quantum evolution. *Phys. Rev. Lett.* **65**, 1697–1700 (1990).
- Provost, J. P. & Vallee, G. Riemannian structure on manifolds of quantum states. *Commun. Math. Phys.* **76**, 289–301 (1980).
- Mera, B. & Ozawa, T. Kähler geometry and chern insulators: relations between topology and the quantum metric. *Phys. Rev. B* **104**, 045104 (2021).
- Thouless, D. J., Kohmoto, M., Nightingale, M. P. & den Nijs, M. Quantized Hall conductance in a two-dimensional periodic potential. *Phys. Rev. Lett.* **49**, 405–408 (1982).
- Haldane, F. D. M. Berry curvature on the Fermi surface: anomalous Hall effect as a topological Fermi-liquid property. *Phys. Rev. Lett.* **93**, 206602 (2004).
- Nagaosa, N., Sinova, J., Onoda, S., MacDonald, A. H. & Ong, N. P. Anomalous Hall effect. *Rev. Mod. Phys.* **82**, 1539–1592 (2010).
- Groenendijk, D. J. et al. Berry phase engineering at oxide interfaces. *Phys. Rev. Res.* **2**, 023404 (2020).
- van Thiel, T. et al. Coupling charge and topological reconstructions at polar oxide interfaces. *Phys. Rev. Lett.* **127**, 127202 (2021).
- Lv, B. Q. et al. Experimental discovery of Weyl semimetal TaAs. *Phys. Rev. X* **5**, 031013 (2015).
- Nandy, S., Sharma, G., Taraphder, A. & Tewari, S. Chiral anomaly as the origin of the planar Hall effect in Weyl semimetals. *Phys. Rev. Lett.* **119**, 176804 (2017).
- Armitage, N. P., Mele, E. J. & Vishwanath, A. Weyl and Dirac semimetals in three-dimensional solids. *Rev. Mod. Phys.* **90**, 015001 (2018).
- Battilomo, R., Scopigno, N. & Ortix, C. Anomalous planar Hall effect in two-dimensional trigonal crystals. *Phys. Rev. Res.* **3**, L012006 (2021).
- Cullen, J. H., Bhalla, P., Marcellina, E., Hamilton, A. R. & Culcer, D. Generating a topological anomalous Hall effect in a nonmagnetic conductor: an in-plane magnetic field as a direct probe of the Berry curvature. *Phys. Rev. Lett.* **126**, 256601 (2021).
- Deyo, E., Golub, L. E., Ivchenko, E. L. & Spivak, B. Semiclassical theory of the photogalvanic effect in non-centrosymmetric systems. Preprint at [arXiv https://arxiv.org/abs/0904.1917](https://arxiv.org/abs/0904.1917) (2009).
- Moore, J. E. & Orenstein, J. Confinement-induced Berry phase and helicity-dependent photocurrents. *Phys. Rev. Lett.* **105**, 026805 (2010).
- Sodemann, I. & Fu, L. Quantum nonlinear Hall effect induced by Berry curvature dipole in time-reversal invariant materials. *Phys. Rev. Lett.* **115**, 216806 (2015).
- Ortix, C. Nonlinear Hall effect with time-reversal symmetry: theory and material realizations. *Adv. Quantum Technol.* **4**, 2100056 (2021).
- Du, Z. Z., Wang, C. M., Li, S., Lu, H.-Z. & Xie, X. C. Disorder-induced nonlinear Hall effect with time-reversal symmetry. *Nat. Commun.* **10**, 3047 (2019).
- Soluyanov, A. A. et al. Type-II Weyl semimetals. *Nature* **527**, 495–498 (2015).
- Singh, S., Kim, J., Rabe, K. M. & Vanderbilt, D. Engineering Weyl phases and nonlinear Hall effects in T_d -MoTe₂. *Phys. Rev. Lett.* **125**, 046402 (2020).
- Koepf, K. et al. TaTe₄: a ternary type-II Weyl semimetal. *Phys. Rev. B* **93**, 201101 (2016).
- Kumar, D. et al. Room-temperature nonlinear Hall effect and wireless radio-frequency rectification in Weyl semimetal TaTe₄. *Nat. Nanotechnol.* **16**, 421–425 (2021).
- Facio, J. I. et al. Strongly enhanced Berry dipole at topological phase transitions in BiTeI. *Phys. Rev. Lett.* **121**, 246403 (2018).
- Nandy, S. & Sodemann, I. Symmetry and quantum kinetics of the nonlinear Hall effect. *Phys. Rev. B* **100**, 195117 (2019).
- Hsieh, T. H. et al. Topological crystalline insulators in the snite material class. *Nat. Commun.* **3**, 982 (2012).
- Lau, A. & Ortix, C. Topological semimetals in the SnTe material class: Nodal lines and Weyl points. *Phys. Rev. Lett.* **122**, 186801 (2019).
- Xu, S.-Y. et al. Electrically switchable Berry curvature dipole in the monolayer topological insulator WTe₂. *Nat. Phys.* **14**, 900–906 (2018).
- You, J.-s., Fang, S., Xu, S.-y., Kaxiras, E. & Low, T. Berry curvature dipole current in the transition metal dichalcogenides family. *Phys. Rev. B* **98**, 121109 (2018).
- Kang, K., Li, T., Sohn, E., Shan, J. & Mak, K. F. Nonlinear anomalous Hall effect in few-layer WTe₂. *Nat. Mater.* **18**, 324–328 (2019).
- Ma, Q. et al. Observation of the nonlinear Hall effect under time-reversal-symmetric conditions. *Nature* **565**, 337–342 (2019).
- Du, Z. Z., Wang, C. M., Lu, H.-Z. & Xie, X. C. Band signatures for strong nonlinear Hall effect in bilayer WTe₂. *Phys. Rev. Lett.* **121**, 266601 (2018).

33. Ho, S.-C. et al. Hall effects in artificially corrugated bilayer graphene without breaking time-reversal symmetry. *Nat. Electron.* **4**, 116–125 (2021).
34. Battilomo, R., Scopigno, N. & Ortix, C. Berry curvature dipole in strained graphene: a Fermi surface warping effect. *Phys. Rev. Lett.* **123**, 196403 (2019).
35. He, P. et al. Quantum frequency doubling in the topological insulator Bi_2Se_3 . *Nat. Commun.* **12**, 698 (2021).
36. Lesne, E. et al. Designing spin and orbital sources of berry curvature at oxide interfaces <https://doi.org/10.1038/s41563-023-01498-0> (2022). (in press).
37. He, P. et al. Observation of out-of-plane spin texture in a $\text{SrTiO}_3(111)$ two-dimensional electron gas. *Phys. Rev. Lett.* **120**, 266802 (2018).
38. Trama, M., Cataudella, V., Perroni, C. A., Romeo, F. & Citro, R. Gate tunable anomalous Hall effect: Berry curvature probe at oxides interfaces. *Phys. Rev. B* **106**, 075430 (2022).
39. Fu, L. Hexagonal warping effects in the surface states of the topological insulator Bi_2Te_3 . *Phys. Rev. Lett.* **103**, 266801 (2009).
40. Nielsen, H. & Ninomiya, M. A no-go theorem for regularizing chiral fermions. *Phys. Lett. B* **105**, 219–223 (1981).
41. Hasan, M. Z. & Kane, C. L. Colloquium: Topological insulators. *Rev. Mod. Phys.* **82**, 3045–3067 (2010).
42. Zhang, S.-C. et al. Topological insulators in Bi_2Se_3 , Bi_2Te_3 and Sb_2Te_3 with a single Dirac cone on the surface. *Nat. Phys.* **5**, 438–442 (2009).
43. Hsieh, D. et al. Observation of time-reversal-protected single-Dirac-cone topological-insulator states in Bi_2Te_3 and Sb_2Te_3 . *Phys. Rev. Lett.* **103**, 146401 (2009).
44. Xiao, D., Chang, M.-C. & Niu, Q. Berry phase effects on electronic properties. *Rev. Mod. Phys.* **82**, 1959–2007 (2010).
45. Park, S. R., Kim, C. H., Yu, J., Han, J. H. & Kim, C. Orbital-angular-momentum based origin of Rashba-type surface band splitting. *Phys. Rev. Lett.* **107**, 156803 (2011).
46. B. Kim, B. et al. Microscopic mechanism for asymmetric charge distribution in Rashba-type surface states and the origin of the energy splitting scale. *Phys. Rev. B* **88**, 205408 (2013).
47. Mercaldo, M. T., Solinas, P., Giazotto, F. & Cuoco, M. Electrically tunable superconductivity through surface orbital polarization. *Phys. Rev. Appl.* **14**, 034041 (2020).
48. Barnett, R., Boyd, G. R. & Galitski, V. SU(3) spin-orbit coupling in systems of ultracold atoms. *Phys. Rev. Lett.* **109**, 235308 (2012).
49. Liu, C.-X. et al. Model Hamiltonian for topological insulators. *Phys. Rev. B* **82**, 045122 (2010).
50. Green, D., Santos, L. & Chamon, C. Isolated flat bands and spin-1 conical bands in two-dimensional lattices. *Phys. Rev. B* **82**, 075104 (2010).
51. Giovannetti, G., Capone, M., van den Brink, J. & Ortix, C. Kekulé textures, pseudospin-one Dirac cones, and quadratic band crossings in a graphene-hexagonal indium chalcogenide bilayer. *Phys. Rev. B* **91**, 121417 (2015).
52. Fang, C. & Fu, L. New classes of topological crystalline insulators having surface rotation anomaly. *Sci. Adv.* **5**, eaat2374 (2019).
53. Monteiro, A. M. R. V. L. et al. Band inversion driven by electronic correlations at the (111) $\text{LaAlO}_3/\text{SrTiO}_3$ interface. *Phys. Rev. B* **99**, 201102 (2019).
54. Khanna, U. et al. Symmetry and correlation effects on band structure explain the anomalous transport properties of (111) $\text{LaAlO}_3/\text{SrTiO}_3$. *Phys. Rev. Lett.* **123**, 036805 (2019).
55. Liu, C. et al. Two-dimensional superconductivity and anisotropic transport at $\text{KTaO}_3(111)$ interfaces. *Science* **371**, 716–721 (2021).
56. Reyren, N. et al. Superconducting interfaces between insulating oxides. *Science* **317**, 1196–1199 (2007).
57. De Luca, G. M. et al. Symmetry breaking at the (111) interfaces of SrTiO_3 hosting a two-dimensional electron system. *Phys. Rev. B* **98**, 115143 (2018).
58. Fleury, P. A., Scott, J. F. & Worlock, J. M. Soft phonon modes and the 110°k phase transition in SrTiO_3 . *Phys. Rev. Lett.* **21**, 16–19 (1968).
59. Salje, E. K. H., Aktas, O., Carpenter, M. A., Laguta, V. V. & Scott, J. F. Domains within domains and walls within walls: evidence for polar domains in cryogenic SrTiO_3 . *Phys. Rev. Lett.* **111**, 247603 (2013).
60. Rössle, M. et al. Electric-field-induced polar order and localization of the confined electrons in $\text{LaAlO}_3/\text{SrTiO}_3$ heterostructures. *Phys. Rev. Lett.* **110**, 136805 (2013).
61. Graf, A. & Piéchon, F. Berry curvature and quantum metric in N -band systems: an eigenprojector approach. *Phys. Rev. B* **104**, 085114 (2021).
62. Go, D., Jo, D., Lee, H.-W., Kläui, M. & Mokrousov, Y. Orbitronics: orbital currents in solids. *Europhys. Lett.* **135**, 37001 (2021).

ACKNOWLEDGEMENTS

A.D.C., M.C., and M.T.M. acknowledge support by the EU's Horizon 2020 research and innovation program under Grant Agreement No. 964398 (SUPERGATE). A.D.C. acknowledges support by the Swiss State Secretariat for Education, Research and Innovation (SERI) under contract number MB22.00071, by the Gordon and Betty Moore Foundation (Grant No. 332 GBMF10451 to A.D.C.) and by the Netherlands Organisation for Scientific Research (NWO/OCW) as part of the VIDi [project 016.Vidi.189.061] and ENW-GROOT [project TOPCORE] programs. We thank M. Gabay for valuable discussions.

AUTHOR CONTRIBUTIONS

C.O. conceived and supervised the project. M.T.M. performed the computations with help from C.N. and M.C. M.T.M., C.N., A.C., M.C. and C. O. analysed the results and wrote the manuscript.

COMPETING INTERESTS

The authors declare no competing interests.

ADDITIONAL INFORMATION

Supplementary information The online version contains supplementary material available at <https://doi.org/10.1038/s41535-023-00545-y>.

Correspondence and requests for materials should be addressed to Maria Teresa Mercaldo or Carmine Ortix.

Reprints and permission information is available at <http://www.nature.com/reprints>

Publisher's note Springer Nature remains neutral with regard to jurisdictional claims in published maps and institutional affiliations.



Open Access This article is licensed under a Creative Commons Attribution 4.0 International License, which permits use, sharing, adaptation, distribution and reproduction in any medium or format, as long as you give appropriate credit to the original author(s) and the source, provide a link to the Creative Commons license, and indicate if changes were made. The images or other third party material in this article are included in the article's Creative Commons license, unless indicated otherwise in a credit line to the material. If material is not included in the article's Creative Commons license and your intended use is not permitted by statutory regulation or exceeds the permitted use, you will need to obtain permission directly from the copyright holder. To view a copy of this license, visit <http://creativecommons.org/licenses/by/4.0/>.

© The Author(s) 2023